A&A 546, A68 (2012)
DOI: 10.1051/0004-6361/201118052
© ESO 2012

Astronomy & Astrophysics

Winds of change – a molecular outflow in NGC 1377?

The anatomy of an extreme FIR-excess galaxy

S. Aalto[1], S. Muller[1], K. Sakamoto[2], J. S. Gallagher[3], S. Martín[4], and F. Costagliola[1]

[1] Department of Earth and Space Sciences, Chalmers University of Technology, Onsala Observatory, 43994 Onsala, Sweden
e-mail: saalto@chalmers.se
[2] Institute of Astronomy and Astrophysics, Academia Sinica, PO Box 23-141, 10617 Taipei, Taiwan
[3] Department of Astronomy, University of Wisconsin-Madison, 5534 Sterling, 475 North Charter Street, Madison, WI 53706, USA
[4] European Southern Observatory, Alonso de Córdova 3107, Vitacura, Casilla, 19001, Santiago 19, Chile

Received 8 September 2011 / Accepted 13 June 2012

ABSTRACT

Aims. Our goal was to investigate the molecular gas distribution and kinematics in the extreme far-infrared (FIR) excess galaxy NGC 1377 and to address the nature and evolutionary status of the buried source.

Methods. We used high- ($0\farcs65 \times 0\farcs52$, ($65 \times 52$ pc)) and low- ($4\farcs88 \times 2\farcs93$) resolution SubMillimeter Array (SMA) observations to image the ^{12}CO and ^{13}CO 2−1 line emission.

Results. We find bright, complex ^{12}CO 2−1 line emission in the inner 400 pc of NGC 1377. The ^{12}CO 2−1 line has wings that are tracing a kinematical component that appears to be perpendicular to the component traced by the line core. Together with an intriguing X-shape of the integrated intensity and dispersion maps, this suggests that the molecular emission of NGC 1377 consists of a disk-outflow system. Lower limits to the molecular mass and outflow rate are $M_{\rm out}({\rm H_2}) > 1 \times 10^7\ M_\odot$ and $\dot{M} > 8\ M_\odot\,{\rm yr}^{-1}$. The age of the proposed outflow is estimated to be 1.4 Myr, the extent to be 200 pc and the outflow speed to be $V_{\rm out} = 140$ km s^{-1}. The total molecular mass in the SMA map is estimated to $M_{\rm tot}({\rm H_2}) = 1.5 \times 10^8\ M_\odot$ (on a scale of 400 pc) while in the inner $r = 29$ pc the molecular mass is $M_{\rm core}({\rm H_2}) = 1.7 \times 10^7\ M_\odot$ with a corresponding H_2 column density of $N({\rm H_2}) = 3.4 \times 10^{23}$ cm^{-2} and an average ^{12}CO 2−1 brightness temperature of 19 K. ^{13}CO 2−1 emission is found at a factor 10 fainter than ^{12}CO in the low-resolution map while C^{18}O 2−1 remains undetected. We find weak 1 mm continuum emission of 2.4 mJy with spatial extent less than 400 pc.

Conclusions. Observing the molecular properties of the FIR-excess galaxy NGC 1377 allows us to probe the early stages of nuclear activity and the onset of feedback in active galaxies. The age of the outflow supports the notion that the current nuclear activity is young – a few Myr. The outflow may be powered by radiation pressure from a compact, dust enshrouded nucleus, but other driving mechanisms are possible. The buried source may be an active galactic nucleus (AGN) or an extremely young (1 Myr) compact starburst. Limitations on size and mass lead us to favor the AGN scenario, but additional studies are required to settle this question. In either case, the wind with its implied mass outflow rate will quench the nuclear power source within the very short time of 5−25 Myr. It is possible, however, that the gas is unable to escape the galaxy and may eventually fall back onto NGC 1377 again.

Key words. galaxies: evolution – galaxies: individual: NGC 1377 – galaxies: active – galaxies: starburst – radio lines: ISM – ISM: molecules

1. Introduction

A small subset of galaxies deviate strongly from the well-known radio to far-infrared (FIR) correlation because they have a higher FIR than radio emission ($q > 3$; $q = \log[{\rm FIR}/3.75 \times 10^{12}\ {\rm Hz}]/S_\nu(1.4\ {\rm GHz}$, Helou et al. 1985). There are several potential interpretations of the excess, including very young synchrotron-deficient starbursts or dust-enshrouded active galactic nuclei (AGN). These AGN obscured by nuclear dust are likely also in the early stages of their evolution where nuclear material has not yet been dispersed and/or consumed to feed the growth of the black hole. The FIR-excess galaxies are rare – Roussel et al. (2003) found that they represent a small fraction (1%) of an infrared flux-limited sample in the local universe, such as the IRAS Faint Galaxy Sample. Despite their scarcity, which likely is an effect of the short time spent in the FIR-excess phase, these objects deserve careful study. Their implied youth provides an ideal setting to better understand the initial conditions and early evolution of starburst and/or AGN activity, as well as insights into how the infrared and radio emission is regulated in galaxies.

1.1. The extreme FIR-excess galaxy NGC 1377

NGC 1377 is a member of the Eridanus galaxy group at an estimated distance of 21 Mpc (1″ = 102 pc) and has a FIR luminosity of $L_{\rm FIR} = 4.3 \times 10^9\ L_\odot$ (Roussel et al. 2003). In stellar light, NGC 1377 has the appearance of a regular lenticular galaxy (de Vaucouleurs et al. 1991), with a diameter of 1′.8, a large-scale inclination of 60° and a major axis position angle (PA) of 92° (as derived from the K-band image). However, Heisler & Vader (1994) reported the presence of a faint dust lane along the southern part of the minor axis, perturbing an otherwise featureless morphology. NGC 1377 is a sixty micron peaker (SMP) – meaning that its IR spectral energy distribution (SED) peaks near 60 μm. The SMPs are often found to have peculiar morphologies and are either classified as H II-region-like or Sy 2 – where the Sy 2 are somewhat more common (e.g. Heisler & Vader 1994; Laureijs et al. 2000).

NGC 1377 is *the most extreme example known so far of the FIR-excess galaxies.* Its radio synchrotron emission is deficient by at least a factor of 37 with respect to normal galaxies (Roussel et al. 2003, 2006) (corresponding to $q > 3.92$). Interestingly,

H II regions were not detected through near-infrared hydrogen recombination lines or thermal radio continuum (Roussel et al. 2003, 2006). The presence of cold molecular gas in the center of NGC 1377 is evident through bright single-dish ^{12}CO 1−0 and 2−1 line emission detected by Roussel et al. (2003). Deep mid-infrared silicate absorption features suggest that the nucleus is enshrouded by large masses of dust (e.g. Spoon et al. 2007), which potentially absorb all ionizing photons. The extremely high obscuration hampers the determination of the nature of the nuclear activity.

Roussel et al. (2006) proposed that NGC 1377 is a nascent ($t \lesssim 1$ Myr) opaque starburst – the radio synchrotron deficiency would then be caused by the extreme youth (pre-supernova stage) of the starburst activity where the young stars are still embedded in their birth-clouds. In contrast, Imanishi (2006) argued, based on the small 3.3 μm PAH equivalent widths and very red L-band continuum, that NGC 1377 harbors a buried AGN. Furthermore, Imanishi et al. (2009) found an HCN/HCO$^+$ J = 1−0 line ratio exceeding unity, which they suggested is evidence of an X-ray dominated region (XDR) surrounding an AGN. The authors explained the lack of radio continuum by suggesting the presence of a large column of intervening material that cause free-free absorption. Note, however, that the HCN/HCO$^+$ line ratio determination of the XDR contribution is uncertain and is based on small differences in the ratios (see e.g. Fig. 5 in Krips et al. 2008). Furthermore, the lack of a thermal radio continuum detection also sets limits on the possibility of nuclear free-free absorption.

To further our understanding of the nature of NGC 1377 we obtained high-resolution ^{12}CO and ^{13}CO 2−1 data with the SubMillimeter Array (SMA) in Hawaii. Because NGC 1377 remains undetected in HI and Hα according to reports in the literature[1] (Roussel et al. 2003, 2006) the molecular lines seem to be an important way to study the gas properties and dynamics. Our goal was to search for clues to the extreme FIR-excess of NGC 1377 through the distribution and kinematics of the molecular gas. We found evidence of a molecular disk-outflow system and we used its properties to address the nature of the buried source.

In Sect. 2 we present the observations and results which are discussed in terms of the structure and power of a molecular disk-outflow system in Sects. 3.1 and 3.2. In Sect. 3.3 possible power sources of the outflow are presented and in Sect. 3.4 we briefly compare our results with molecular outflows in the literature. The properties of the nuclear gas are discussed in Sect. 3.5 and evolutionary implications for NGC 1377 are considered in Sect. 3.6.

2. Observations and results

NGC 1377 was observed with the SubMillimeter Array (SMA) on 2009 July 17, in the very extended configuration (eight antennas), and on 2009 October 12, in the compact configuration (seven antennas). The phase center was set at α = 03:36:39.10 and δ = −20:54:08.0 (J2000). During both nights, the zenith atmospheric opacity at 225 GHz was near 0.1, resulting in system temperatures in the range 100−200 K depending on source elevation.

[1] Gallagher et al. (in prep.) obtained a spectrum with the Southern African Large Telescope (SALT) that shows emission for Hα and [N II], and we therefore assume that these lines, along with the previously measured [S II] double, are weak but present in NGC 1377.

The heterodyne SIS receivers were tuned to the frequency of the ^{12}CO 2−1 transition at 230.538 GHz in the upper sideband, while the ^{13}CO 2−1 transition was observed in the lower sideband. The correlator was configured to provide a spectral resolution of 0.8125 MHz.

The bandpass of the individual antennas was derived from the bright quasars J1924−292 in July, and 3C 454.3 in October. The primary flux calibration was set on Callisto and Uranus, respectively. The close-by quasars J0423-013 (~4 Jy at 1 mm) and J0334-401 (~1.3 Jy) were observed regularly for complex gain calibration, every 15 min for observations in the very extended configuration, and every 25 min for the compact configuration. We derived a flux density for J0423-013 of 3.3 Jy in July and 4.5 Jy in October and for J0334-401 the derived flux density was 1.2 Jy in July and 1.4 Jy in October. The quasar J0340-213, closer to NGC 1377 (1° away) but weaker (~0.4 Jy) than J0423-013 and J0334-401 was also observed during the very extended configuration track for calibration-testing purpose: after the gain solution derived from J0423-013 and J0334-401 was applied to J0340-213, it was found with no measurable offsets relative to its known position, and with a consistent flux, making us confident with the calibration of our very extended configuration data.

After calibration within the dedicated MIR/IDL SMA reduction package, both visibility sets were converted into FITS format, and imported in the GILDAS/MAPPING and AIPS packages for further imaging.

2.1. ^{12}CO 2–1 emission

For the ^{12}CO 2−1 data, sets of visibilities were combined and deconvolved using the Clark method with uniform weighting. This results in a synthesized beam size of 0.″65 × 0.″52 with position angle PA = 8°. We smoothed the data to a velocity resolution of 5 km s^{-1}, yielding a 1σ rms noise level of 16 mJy beam^{-1}.

Furthermore, data taken with the compact array were also deconvolved with natural weighting resulting in a synthesized beam size of 4.″88 × 2.″93 (PA = 176°)(1σ rms noise level of 23 mJy beam^{-1}). This provides a low-resolution map to which we compared the high-resolution data.

The integrated intensity maps, velocity fields and dispersion maps are presented in Fig. 1 and the high-resolution channel maps are shown in Fig. 2.

2.1.1. The integrated ^{12}CO 2–1 intensity and molecular mass

In the high-resolution map (Fig. 1, top left) the molecular emission is resolved and arises mostly from a region of 1″ (100 pc at D = 21 Mpc) in radius. (From a Gaussian fit we find a full width half maximum (FWHM) major axis of 1.″76 and minor axis 1.″4.) Fainter emission extends out to a radius of 2−3″. The integrated emission structure is quite complex with various filamentary features extending out from the center. A tilted X-like shape appears to emerge from the center. In the low-resolution map the emission is mostly unresolved, but some faint emission is extending to the west and northeast from the central condensation.

The integrated intensities and estimated molecular masses are presented in Table 1. The H_2 column density toward the inner D = 58 pc (average beam diameter) is estimated to be $N(H_2) = 3.4 \times 10^{23}$ cm^{-2}, leading to an average nuclear molecular gas surface density of $\Sigma \approx 5 \times 10^3$ $M_\odot$ pc^{-2}. The average column density for the central 390 pc is $\approx 5 \times 10^{22}$ cm^{-2}. Please

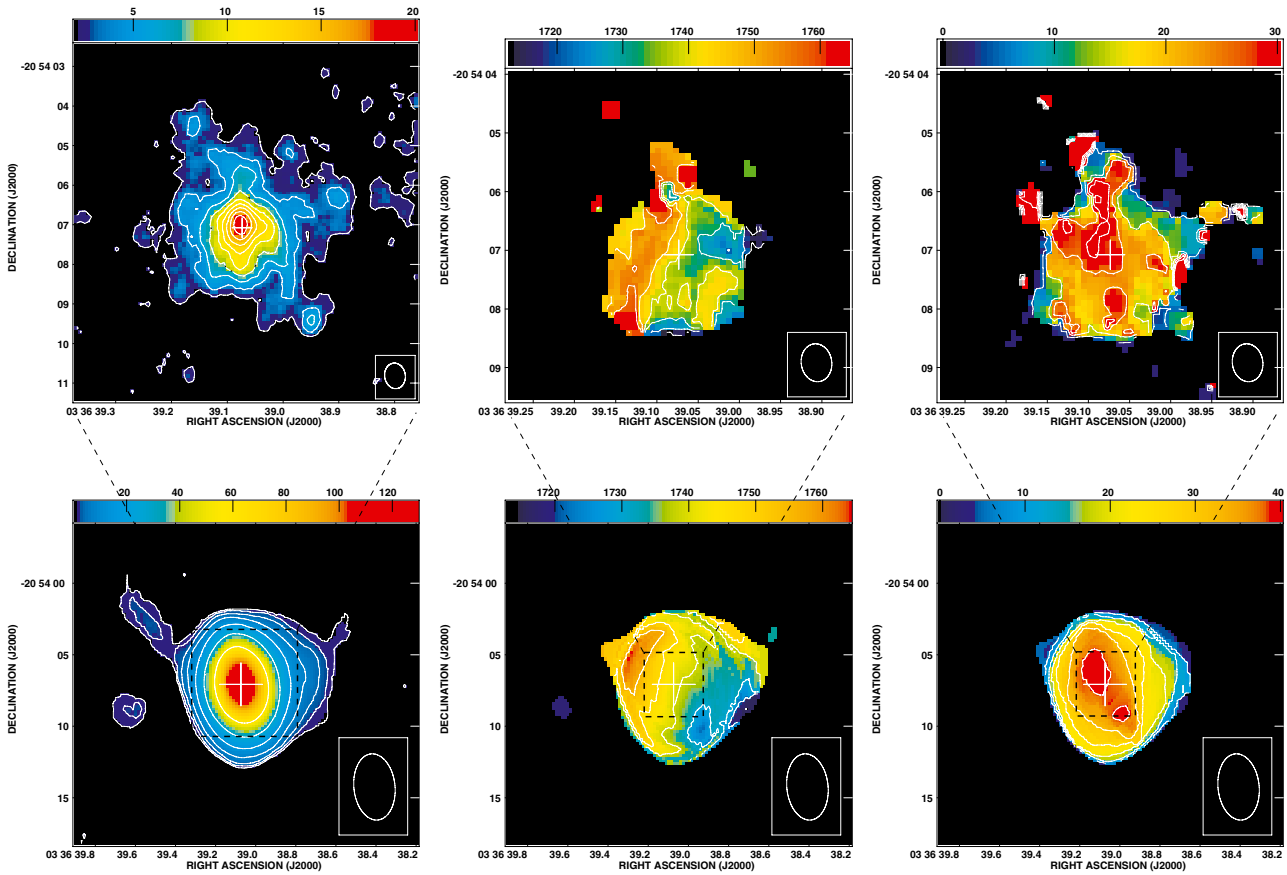

Fig. 1. *Top panels*: high-resolution moment maps of ^{12}CO 2−1. *Left*: integrated intensity with contour levels 2 × (1,2, 3, 4, 5, 6, 7, 8, 9) Jy beam^{-1} km s^{-1} and grayscale ranging from 2 to 20 Jy beam^{-1} km s^{-1}. The cross marks the position α: 03:36:39.073 δ: –20:54:07.08, which is the position of peak $T_{\rm B}$(^{12}CO 2−1). *Center*: velocity field with contour levels starting at 1713 km s^{-1} and then increasing by steps of 8.6 km s^{-1}. The grayscale ranges from 1713 to 1764 km s^{-1}. *Right*: dispersion map where contours start at 5 km s^{-1} and then increase by steps of 10 km s^{-1}. Grayscale ranges from 0 to 30 km s^{-1} and peak dispersion is 90 km s^{-1}. *Lower panels*: low-resolution moment maps of ^{12}CO 2−1. *Left*: integrated intensity with contour levels 0.9 × (1, 2, 4, 8, 16, 32, 64) Jy beam^{-1} km s^{-1} and grayscale ranging from 0 to 129 Jy beam^{-1} km s^{-1}. *Center*: velocity field with contour levels starting at 1713 km s^{-1} and then increasing by steps of 8.6 km s^{-1}. The grayscale ranges from 1713 to 1764 km s^{-1}. *Right*: dispersion map where contours start at 8.6 km s^{-1} and then increase by steps of 6.4 km s^{-1}. Grayscale ranges from 0 to 40 km s^{-1} and peak dispersion is 65 km s^{-1}. Note that the high-resolution moment 1 and 2 maps are on a somewhat different scale compared to the moment 0 map to better show the details of the velocity field and dispersion map. (In the online version of this figure the grayscale is replaced with a rainbow color scale ranging from dark blue to red.)

see footnote to Table 1 for ^{12}CO to H_2 mass conversion. Potential errors are discussed in more detail in Sect. 3.1.3.

We investigated what fraction of the single-dish flux was recovered with our interferometric observations by comparing them with our IRAM 30 m ^{12}CO 2−1 observations. We find a ^{12}CO 2−1 luminosity in the 9″ IRAM beam of 3.5 × 10^7 K km s^{-1} pc^2, to be compared to the SMA total ^{12}CO luminosity of 3.3 × 10^7 K km s^{-1} pc^2. Within the errors we conclude that the whole IRAM 30 m flux has been recovered with the interferometer.

2.1.2. Kinematics

Velocity field: The high-resolution velocity field (Fig. 1, top center) shows complex dynamics dominated by redshifted gas to the east of the center and blueshifted gas to the west. Fitted velocity centroids range from 1690 to 1770 km s^{-1}. In the low-resolution map, the position angle of the smoother velocity field is dominated by a PA ≈ 40° component and velocity centroids range from 1712 to 1764 km s^{-1}. The velocity centroids were determined through a flux-weighted first moment of the spectrum of each pixel, therefore assigning one velocity to a potentially complex spectral structure.

Dispersion maps: The high-resolution dispersion map (Fig. 1, top right) shows a distinct X-like shape – where the "x" itself has a PA of 35°–40°. Dispersion (one dimensional, σ_{1d}) in the X-structure is typically 25 km s^{-1}, but – reaches 44 km s^{-1} or higher in isolated regions. The high dispersion is caused by multiple, narrow, spectral features and/or broad wing-like components. The low-resolution dispersion map shows a less complicated pattern where the dispersion is dominated by a bipolar large-scale feature with peaks of σ_{1d} = 40 km s^{-1}. The dispersion was determined through a flux-weighted second moment of the spectrum of each pixel. This corresponds to the one-dimensional velocity dispersion (i.e. the FWHM line width of the spectrum divided by 2.35 for a Gaussian line profile).

Spectra and channel map: The low-resolution integrated ^{12}CO 2−1 spectrum is characterized by narrow emission at the line center with FWHM line width δV ≈ 60 km s^{-1} and by triangular-shaped wings (or plateau) ranging from 1620 km s^{-1} to 1860 km s^{-1} (see Fig. 3 top panel). Wings are therefore

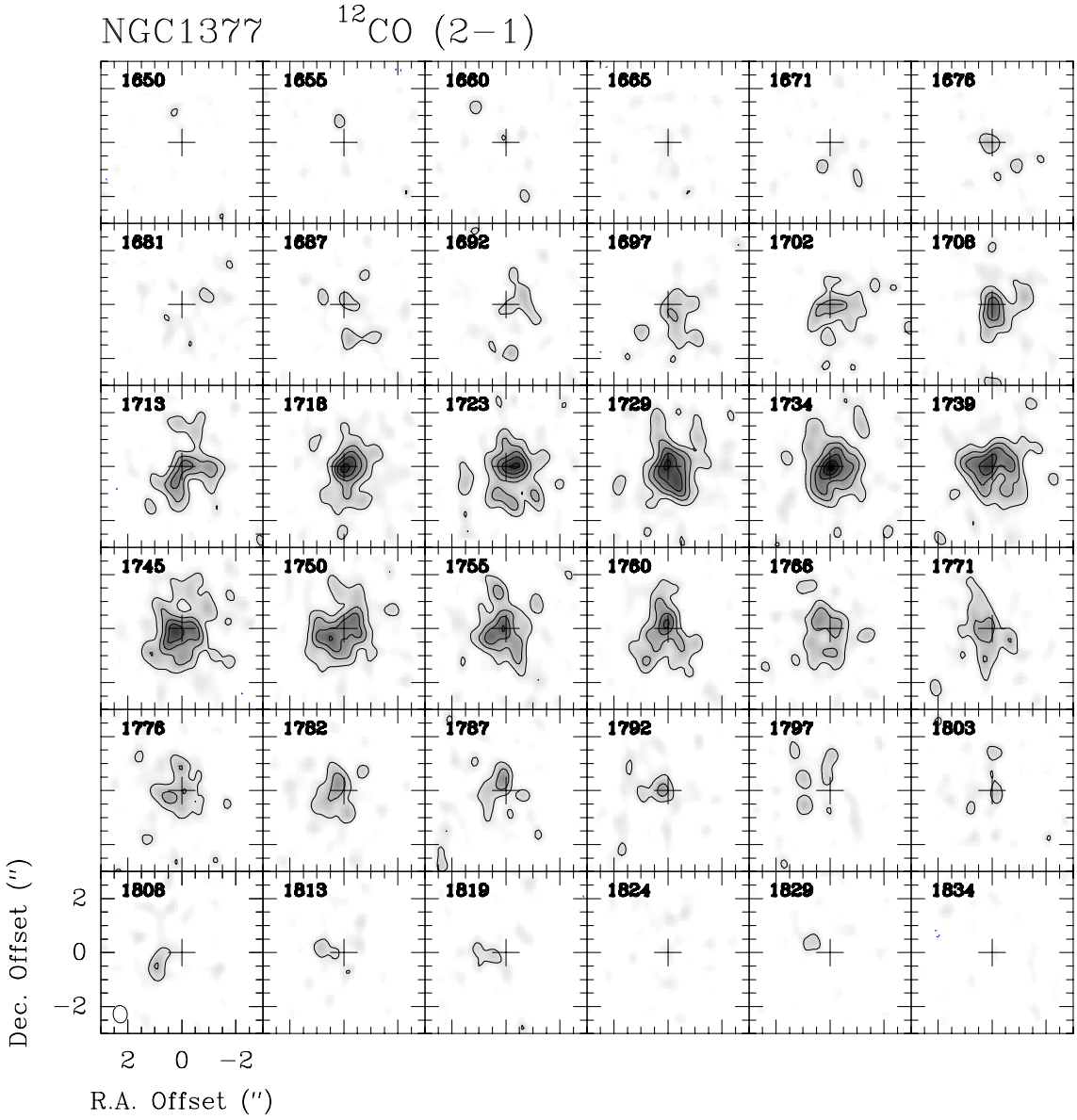

Fig. 2. High-resolution channel map of the ^{12}CO 2−1 emission toward NGC 1377, as obtained from the combination of the compact and very extended configuration data. Contours are drawn every 48 mJy beam^{-1} (3σ). The synthesized beam of 0.″65 × 0.″52 is shown in the bottom left corner.

stretching out to ±120 km s^{-1} (projected). This line shape is also seen in the SEST single-dish ^{12}CO 1−0 spectrum by Roussel et al. (2003). The high-resolution channel map reveals significant structure and complexity in the ^{12}CO 2−1 line emission per channel. Note that there is no evidence of a bright, broad compact emission from an unresolved nuclear source. Brightest line emission in terms of peak $T_{\rm B}$ (19 K) occurs at V = 1734 km s^{-1} which we adopted as the center velocity.

Line wings: To identify the spatial origin of the line wings, we integrated the emission corresponding to velocities 1660−1676 km s^{-1} (blue wings) and 1813−1829 km s^{-1} (red wings) ($V_{\rm sys}$ = 1734 km s^{-1}) in the low-resolution ^{12}CO 2−1 data. The resulting map is presented as the top left panel of Fig. 4. The blue and red wings are spatially separated by ≈2″ and with a PA of 45°. In the lower left panel of Fig. 4 we present an image from the high-resolution data. Here we have integrated the emission corresponding to the central channels: blue: 1718−1729 km s^{-1} and red: 1739−1750 km s^{-1}. In this figure, we see a velocity shift along an axis perpendicular to the one seen for the line wings of the low-resolution data.

The relative positional uncertainty is on the order of (beam size)/(signal-to-noise ratio). For the low-resolution wing map this is less than 0.″7 and for the high-resolution map it is 0.″05−0.″1. Therefore the two orthogonal velocity gradients are observationally robust.

2.2. ^{13}CO and C^{18}O 2−1 emission

Because the signal-to-noise ratio is lower for ^{13}CO and C^{18}O 2−1, we used only data from the compact configuration, deconvolved using natural weighting and smoothed to a velocity resolution of 11 km s^{-1}. The resulting beam size is 4.″88 × 2.″93 (PA = 176°) and the 1σ rms noise level is 13 mJy beam^{-1}. The low-resolution ^{13}CO and C^{18}O spectra are presented in Fig. 3. The ^{13}CO is clearly detected and a factor of 9−10 fainter than ^{12}CO. C^{18}O is not detected and the ^{12}CO/C^{18}O 2−1 peak

Table 1. ^{12}CO 2–1 flux densities and molecular masses.

Position[a] (J2000)	α: 03:36:39.076 (±0.″2)
	δ: –20:54:07.01 (±0.″1)
Peak flux density[b]	270 ± 16 (mJy beam^{-1})
Flux[c]	
(central beam)	20 ± 0.05 (Jy km s^{-1})
(whole map)	169 ± 0.5 (Jy km s^{-1})
Molecular mass[d]	
(central beam)	1.7×10^7 $M_\odot$
(whole map)	1.5×10^8 $M_\odot$

Notes. The high-resolution ^{12}CO 2–1 data. Listed errors are 1σ rms. [(a)] The position of the ^{12}CO 2–1 integrated intensity. The peak T_B is at α: 03:36:39.073 δ: –20:54:07.08 at V_c = 1734 km s^{-1}. [(b)] The Jy to K conversion in the 0.″65 × 0.52″ beam is 1 K = 14.5 mJy. [(c)] A two-dimensional Gaussian was fitted to the integrated intensity image. [(d)] The ^{12}CO luminosity $L(^{12}\mathrm{CO}) = 18.5 \times D^2 \times (\theta)^2 \times I(^{12}\mathrm{CO})$ K km s^{-1} pc^2 (where D is in Mpc, θ in ″ and $I(^{12}\mathrm{CO})$ in K km s^{-1}) and M(H$_2$) = 3.47$L(^{12}\mathrm{CO})$ for $N(\mathrm{H_2})/I(^{12}\mathrm{CO}) = 2.5 \times 10^{20}$ cm^{-2}). The conversion factor has been calibrated for ^{12}CO 1–0 emission – thus, if the ^{12}CO is subthermally excited, the H$_2$ mass estimated from the 2–1 line should be corrected upward. From our IRAM ^{12}CO 2–1 and 1–0 data we estimate that the 2–1/1–0 line ratio to 0.7 – and hence we corrected masses upward by 30%.

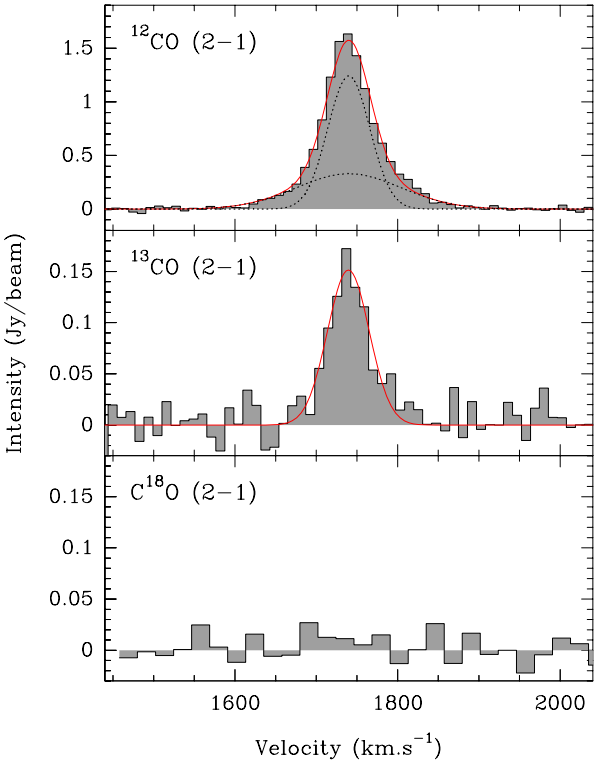

Fig. 3. Spectra of *top panel*: ^{12}CO 2–1, *middle panel*: ^{13}CO 2–1 and *lower panel*: C^{18}O 2–1. All three spectra are taken at position α = 03:36:39.07 δ – 20:54:07.00 in the low-resolution data. ^{13}CO is clearly detected and a factor of 9–10 fainter than ^{12}CO. C^{18}O is not detected and the ^{12}CO/C^{18}O 2–1 peak line intensity ratio is >50. The fits to the ^{12}CO and ^{13}CO spectra are discussed in Sect. 3.1.3.

line intensity ratio is >50. The integrated intensity and velocity field maps are presented in Fig. 5. The peak of the ^{13}CO integrated emission is offset by 0.″9 (90 pc) to the southeast from the peak of the integrated ^{12}CO emission. Furthermore,

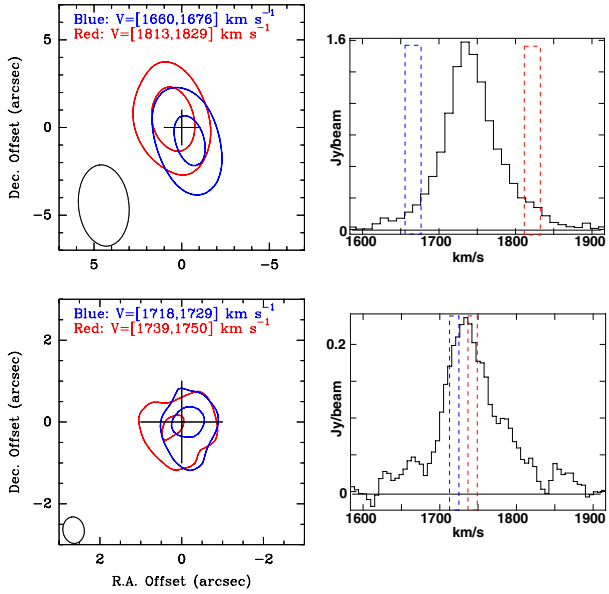

Fig. 4. *Left*: *top panel*: blue (dark) (V = 1660–1676 km s^{-1}) and red (light) (V = 1813–1829 km s^{-1}) showing the location of the wings of the global ^{12}CO spectrum. We used the low-resolution data for maximum sensitivity. *Lower panel*: blue (dark) (V = 1718–1729 km s^{-1}) and red (light) (V = 1739–1750 km s^{-1}) part of the central spectrum of the high-resolution data. The velocities are selected to not overlap with the line wings. Contours are given every 3σ. Two velocity components – perpendicular to each other – can be discerned. *Right*: *top panel*: low-resolution ^{12}CO 2–1 spectrum where the spectral regions in the line wings used to make the figure to the left are indicated. *Lower panel*: high-resolution ^{12}CO 2–1 spectrum where the spectral regions in the line center used to make the figure to the left are indicated. (In the online version of this figure dark contours are blue and light contours are red.)

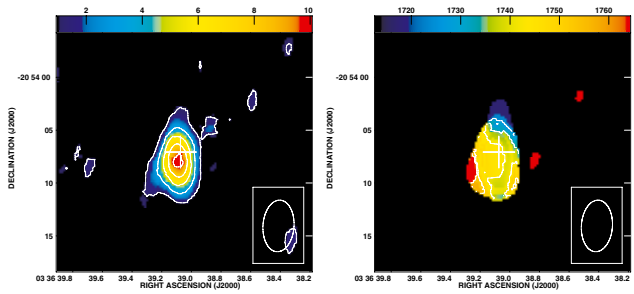

Fig. 5. Low-resolution moment maps of ^{13}CO 2–1. *Left panel*: integrated intensity with contour levels 1.1 × (1, 3, 5, 7, 9, 11) Jy beam^{-1} km s^{-1} and grayscale ranging from 1 to 10 Jy beam^{-1} km s^{-1}. *Right panel*: velocity field with contour levels starting at 1717 km s^{-1} and then increasing by steps of 8.6 km s^{-1}. The grayscale ranges from 1713 to 1764 km s^{-1}. (In the online version of this figure the grayscale is replaced with a rainbow color scale ranging from dark blue to red.)

the ^{13}CO velocity field appears more consistent with that of the high-resolution ^{12}CO data.

2.3. Continuum emission

We detect (4σ) weak 225 GHz continuum in NGC 1377 of 2.4 (±0.45) mJy beam^{-1} in the compact array at the position of the ^{12}CO 2–1 line emission. The source is unresolved in the 4.″88 × 2.″93 beam.

Table 2. Summary of outflow and disk properties.

Outflow	
Molecular mass:	$1.1–5.4 \times 10^7\ M_\odot$
Extent:	200 pc
Orientation:	PA = 35°–45°
Opening angle:	60°–70°
Age:	1.4×10^6 yrs.
Outflow velocity:	140 km s^{-1}
$\dot{M}$:	$8–38\ M_\odot$ yr^{-1}.
Energy:	$2–10 \times 10^{54}$ erg
Power:	$0.4–2 \times 10^{41}$ erg s^{-1}
Nuclear disk	
Diameter:	0.″60 (60 pc)
Orientation:	PA = 110°–130°
Rotational velocity:	75 km s^{-1}
Dynamical mass:	$4 \times 10^7\ M_\odot$
Molecular mass:	$1.7 \times 10^7\ M_\odot$
H_2 column density:	3.4×10^{23} cm^{-2}
H_2 surface density:	$5 \times 10^3\ M_\odot$ pc^{-2}

Notes. Properties are derived and discussed in Sects. 2.1.2, 3.1.1–3.1.4.

3. Discussion

3.1. A molecular outflow?

We propose that the molecular emission of NGC 1377 is dominated by a disk-outflow morphology. *The notion of a molecular outflow is supported by the presence of ^{12}CO 2–1 line wings (Fig. 3) and the spatial orientation of the wing-emission with respect to the line-center emission (Fig. 4). The X-shape of the integrated intensity and dispersion maps (Figs. 1 and 7) is consistent with a biconical outflow structure.* In addition, Roussel et al. (2003) found near-infrared (NIR) H_2(10) S(1) line emission toward the inner 200 pc of NGC 1377 with an orientation of the velocity field similar to the one we found for the ^{12}CO 2–1 line wings. Other alternatives to explain the kinematical structure of the ^{12}CO 2–1 emission include a polar disk or inflowing gas. A polar disk is unlikely since this would require its velocity to be higher than the rotational velocity of the major axis disk. That the kinematics is the signature of an outflow, instead of inflowing gas, is supported by the optical dust absorption feature south of the nucleus visible in Fig. 1 in Roussel et al. (2006). The feature is spatially coincident with the blueshifted line wing, suggesting that the gas on the near side is coming toward us in an outflow. Note that non-circular motions in the galaxy plane may be present and will then add to the complexity of the dynamics.

Below we will discuss the morphology and estimates of molecular mass and velocity of the suggested outflow, but we begin with a brief discussion of the nuclear disk. The fitted properties of the molecular disk-outflow system are summarized in Table 2.

3.1.1. Disk morphology and nuclear dynamical mass

Disk morphology: To further investigate the notion of a disk-outflow system, we made moment maps of only the brightest emission (above 190 mJy beam^{-1}), isolating the narrow-line emission emerging from the inner rotating disk (Fig. 6). Note that the fitted PA of the disk of 110°–130° is consistent with it being perpendicular to the wing emission, the outflow, while the velocity field (right panel) is closer to a PA of ≈95°. This is expected if an outflow is affecting spectral shapes and velocities even close to the nucleus of NGC 1377. The fitted disk diameter ($D(FWHM) = 0.''60$) should be viewed as a lower limit since we used only the top 23% of the emission. The disk inclination is roughly determined to be 45°–70°. Uncertainties largely depend on the difficulty in small-scale separation between disk and outflow components. The stellar large-scale disk is estimated to have an inclination of 60° (from the K-band image) and since it is consistent with the range of values for fits to the nuclear disk, we adopted this value for the nuclear disk as well.

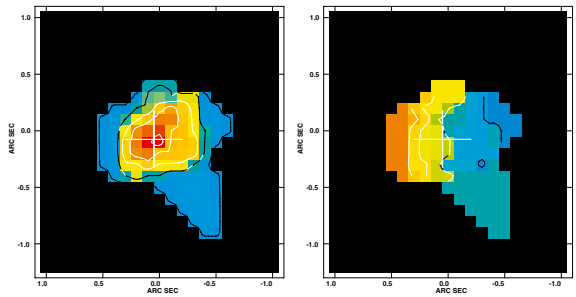

Fig. 6. Integrated intensity and velocity maps of the high-resolution data where only emission in excess of 190 mJy was included to show the location and orientation of the nuclear disk. The position of the cross is the same as in Fig. 1. *Left panel*: integrated intensity where contour levels are 0.72×(1, 3, 5, 7, 9) Jy beam^{-1} km s^{-1} and the grayscale ranges from 0 to 7.2 Jy beam^{-1} km s^{-1}. *Right panel*: velocity field with contour levels starting at 1725 km s^{-1} and then increasing by steps of 5 km s^{-1}. The grayscale ranges from 1720 to 1750 km s^{-1}. The synthesized beam is 0.″65 × 0.″52. (In the online version of this figure the grayscale is replaced with a rainbow color scale ranging from dark blue to red.)

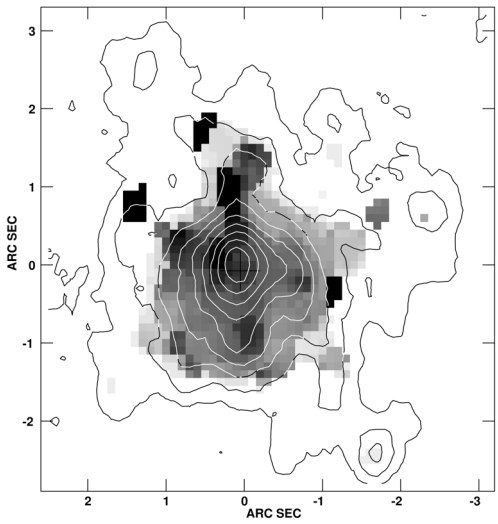

Fig. 7. Overlay of the high-resolution grayscale dispersion map (grayscale ranging from 0 to 34 km s^{-1}) on contours of integrated intensity with contours 2×(1, 2, 3, 4, 5, 6, 7, 8, 9) Jy beam^{-1} km s^{-1}. Note how regions of high dispersion form an X-shaped structure generally aligned with a similar structure in the integrated intensity map.

Disk dynamics: The fitted maximum projected rotational velocity of the disk is 65 km s^{-1} and for an inclination of 60° this results in a $V_{\rm rot}$ of 75 km s^{-1}. The dynamical mass of the 60 pc diameter nuclear disk is estimated to be $M_{\rm dyn} = 4 \times 10^7\ M_\odot$ using the Keplerian formula $M_{\rm dyn} = 2.3 \times 10^8 \times (V_{\rm rot}/100)^2 \times (r/100)$ (where $V_{\rm rot}$ is in km s^{-1} and r in pc). This is only 2.3 times that of

the estimated nuclear molecular mass, implying a relatively high molecular gas mass fraction in the center of ≈40%. A limit to the diameter of the molecular disk (that would be the extension of the nuclear disk) can be set to 200 pc based on the total extent of the SMA high-resolution ^{12}CO 2−1 emission along the disk PA. This is of course sensitivity-limited and a fainter, larger molecular extension to the disk is possible. The Keplerian dynamical mass of this 200 pc disk would be 1.3×10^8 $M_\odot$.

3.1.2. Outflow morphology

The X-shaped morphology of the high-resolution integrated intensity and dispersion maps (see Fig. 7) suggests that the molecular gas outlines a symmetric biconical structure centered on the nucleus. The cone has an opening angle of 60°–70°. Such a large opening angle could explain the complex velocity pattern observed in the high-resolution map. The peak intensity and peak dispersion are roughly correlated in space. The high dispersion may be caused by line-of-sight effects in maximum path-lengths along the cone walls, and also by multiple spectral components where extended disk emission overlaps with emission from the outflowing gas.

Note, however, that the molecular outflow may not be well-collimated or in a simple well-ordered outflow pattern, but instead filamentary and patchy, and the molecular emission is likely a mix of clumpy and extended gas. (Properties of wind-cone structures have been modeled by (e.g.) Tenorio-Tagle & Munoz-Tunon 1998.) The X-shape structure also appears to be evident in the dust morphology of NGC 1377. The optical dust absorption feature south of the nucleus (Fig. 1 in Roussel et al. 2006) shows a V-shape that is spatially coincident with the blue part of the molecular outflow. The redshifted molecular outflow is then hidden behind the galaxy with the blueshifted outflow projected in front of the disk on the southern side.

3.1.3. ^{12}CO luminosity and molecular mass of the outflow

Without a detailed model the ^{12}CO 2–1 luminosity in the outflow is difficult to determine. Below we adopt two approaches to obtain upper and lower limits to the luminosity.

When estimating a *lower limit* to the luminosity in the outflow, we restricted ourselves to the (1628−1655 km s^{-1}) and (1813−1840 km s^{-1}) part of the plateau component (i.e. 79 km s^{-1} $\lesssim |V - V_{\rm sys}| \lesssim$ 106 km s^{-1}) to ensure that the rotational components are not included. We find a flux of 13 ± 0.3 Jy beam^{-1}. Since we only considered a narrow (27 km s^{-1}) part of the 120 km s^{-1} outflow, this is an underestimate of the total ^{12}CO 2−1 flux in the outflow. If the opening angle is as large as we discuss in Sect. 3.1.2, there will be significant projected outflow emission also at systemic velocities.

To obtain an *upper limit* of the outflow luminosity we fit a Gaussian to the line wings in the low-resolution spectrum (see Fig. 3). We first fit a Gaussian to the ^{13}CO 2−1 spectrum (assuming that the ^{13}CO has only a small contribution from the wings) where all parameters are free. We obtained: $S_{\rm peak}$ = 0.15 ± 0.1 Jy beam^{-1}; $V_{\rm c}$ = 1740 ± 2 km s^{-1} and $\delta V(FWHM)$ = 61 ± 5 km s^{-1}. Then, for the ^{12}CO 2−1, we fit two Gaussian curves, using the parameters from the ^{13}CO fitting. The narrow component has $S_{\rm peak}$ = 1.6 ± 0.05 Jy beam^{-1} with $V_{\rm c}$ and δV fixed. The broad component in the wings has, with $V_{\rm c}$ fixed, $S_{\rm peak}$ = 0.4 ± 0.05 Jy beam^{-1} and $\delta V(FWHM)$ = 151 ± 8 km s^{-1} (and the full width of the line wings is ±120 km s^{-1} (projected)). The division of flux between the line core and outflow component is 104 and 65 Jy beam^{-1} km s^{-1} respectively. Because we detected 20 Jy beam^{-1} km s^{-1} in the central high-resolution beam, the narrow component flux is mostly located outside of the inner 0.″6. This flux may be distributed as an extension to the nuclear disk we discuss above in Sect. 3.1.1.

To estimate the molecular mass in the outflow we adopted a standard ^{12}CO-luminosty to $M(H_2)$ conversion factor (see footnote to Table 1). This results in $M(H_2)_{\rm out}$ = 1.1×10^7 $M_\odot$ for the lower limit and for the upper limit $M(H_2)_{\rm out}$ = 5.4×10^7 $M_\odot$. The validity of a standard ^{12}CO to $M(H_2)$ conversion factor in galaxies is heavily debated (e.g. Narayanan et al. 2012; Wada & Tomisaka 2005; Paglione et al. 2001). The global ^{12}CO/^{13}CO 2−1 line intensity ratio of 9−10 suggests that the molecular gas in NGC 1377 is not optically thin (but ^{13}CO limits in the line wings are not sufficient for a reliable line ratio for the highest velocities in the outflow). It is also unclear whether the interferometer would pick up emission that is optically thin since it tends to have low surface brightness. We therefore suggest that applying the conversion factor here does not overestimate gas masses by more than factors of a few.

3.1.4. Mass outflow rate, velocities and acceleration

The projected peak outflow velocity is ∼120 km s^{-1} (Sect. 2.1.2) and if the opening angle of the outflowing gas is ∼60° (and the disk inclination is i = 60°), the actual maximum outflow velocity is ∼140 km s^{-1}. The outflow has reached out to ∼200 pc (corrected for opening angle and inclination) which, for $V_{\rm out}$ = 140 km s^{-1} gives $t_{\rm dyn} = R/V = 1.4 \times 10^6$ yr. The molecular mass in the outflow is $M_{\rm out}$ = 1.1−5.4×10^7 $M_\odot$ (see Sect. 3.1.3). Thus, the molecular mass loss rate $\delta M/\delta t = \dot{M}$ = 8−38 $M_\odot$ yr^{-1}.

We do not know the escape velocity of NGC 1377, hence it is not possible to know whether the gas will leave the system as a whole, or just the nuclear region of NGC 1377. Martin (2005) set a limit for the escape velocity of $V_{\rm esc} = 3V_{\rm rot}$ and if the rotational velocity is 75 km s^{-1}, the gas will not escape NGC 1377.

An inspection of the central spectrum reveals that broad features are present in the very center as well, suggesting that the gas is accelerated close to the nucleus (see lower right panel of Fig. 4). Compared to outflows in M 82 and NGC 253 it appears that the acceleration to the final velocity happens on a comparatively short length scale <30 pc.

3.2. Energy and power of the outflow

We used the prescription by Veilleux et al. (2001) to calculate the kinetic energy in the outflow: $E_{\rm kin} = E_{\rm bulk} + E_{\rm turbulent}$. This kinetic energy represents a lower limit to the energy. The work of lifting the gas out of the nucleus should be included but since we do not know the actual gravitational potential depth of the galaxy, this term cannot be added at this stage. If we assume that the molecular gas in the outflow is moving at constant speed $V_{\rm out}$ = 140 km s^{-1}, we obtain $E_{\rm bulk} = \Sigma_i (1/2)\delta m_i {v_i}^2 = (1/2) M_{\rm out} \times V_{\rm out}^2 \approx 2 \times 10^{54}$ erg – when adopting the lower limit to $M_{\rm out}$. We can however only measure an upper limit to the turbulence of the gas of $\sigma_{\rm 1d}$ = 25 km s^{-1} (due to effects of spatial resolution, rotation and the outflow) and since this term is already lower than the contribution from the bulk motion, we did not include it and in total we estimate $E_{\rm kin}$ to ∼2×10^{54} erg. For the upper limit to $M_{\rm out}$ we obtain $E_{\rm tot} \approx 10^{55}$ erg. The power in the outflow is 0.4–2 × 10^{41} erg s^{-1}, which corresponds to a luminosity of 1–5 × 10^7 $L_\odot$. The ratio between the wind luminosity and the FIR luminosity is then 2×10^{-3}–10^{-2}. From now on we

adopt the more conservative lower value of the luminosity and mass outflow rate.

3.3. What is driving the outflow?

The unusual and obscured nature of NGC 1377 makes it difficult to find an obvious source of the molecular outflow. Is it a buried AGN or a young starburst? Below we investigate some possible scenarios.

3.3.1. Winds from supernovae and massive stars

The limit on L(1.4 GHz) is 5.3×10^{19} W Hz^{-1} (Roussel et al. 2003). This corresponds to an upper limit to the supernova (SN) rate of 5×10^{-4} yr^{-1} (Condon 1992). Inserting this limit into Eqs. (10) and (34) in Murray et al. (2005) we find that the SN rate falls short by an order of magnitude to drive the outflow – by momentum or energy. The lack of radio continuum from SN or supernova remnants (SNR) is consistent with the nondetection of NIR [Fe II] emission by Roussel et al. (2006). However, an outflow may also be driven by the wind-momentum of massive stars. The total momentum in the NGC 1377 outflow is 1.5×10^9 $M_\odot$ km s^{-1}. Using *Starburst99* (Leitherer et al. 1999) we find that a 10^6 $M_\odot$ cluster with a star formation rate (SFR) of 1/3 $M_\odot$ yr^{-1} has a wind-momentum of 10^7 $M_\odot$ km s^{-1} when integrated over 3 Myr. Thus an *SFR* of ~30 $M_\odot$ yr^{-1} would be required. From the FIR luminosity we estimate an *SFR* of 0.4 $M_\odot$ yr^{-1} for NGC 1377 (assuming that the whole FIR is due to star formation) and Roussel et al. (2003) estimate a rate of 1.8 $M_\odot$ yr^{-1}. Thus it appears that the SFR is too low by about one order of magnitude to push out the molecular gas by the wind-momentum of massive stars.

Could the outflow be driven by internal ram pressure from hot gas? Only upper limits to the thermal free-free emission in the radio has been obtained. In Fig. 8 of Roussel et al. (2003) predictions of the radio synchrotron and free-free emission based on the IR are plotted. For NGC 1377 the VLA 1.4 GHz upper limit is about a factor of 4–5 below the expected value. There is thus no direct evidence of much hot ionized gas. Both the Hα and [N II] optical emission lines are weak and Brγ and Paα are undetected (Roussel et al. 2003, 2006). This may be an effect of the high extinction, therefore X-ray observations will be essential to complete the picture of the hot gas of NGC 1377.

Note also that the symmetry of the wind is inconsistent with the idea of external ram pressure driving the wind, as is the presence of NGC 1377 in a low-density galaxy group where ram pressure forces are expected to be low.

3.3.2. Radiation pressure

Murray et al. (2005) suggested that radiation pressure (from both star formation and AGNs) from the continuum absorption and scattering of photons on dust grains may be an efficient mechanism for driving cold, dusty gas out of a galaxy. The lack of evidence for supernovae and the presence of a dusty, compact IR source makes this an attractive scenario for NGC 1377. Murray et al. (2005) proposed that for a radiative pressure-driven outflow the momentum flux $\dot{M}V$ should be comparable to that in the radiation field L/c. For NGC 1377 the outflow momentum flux exceeds L/c by factors of a few, which is within the uncertainties for outflow structure, velocity and mass. We suggest that with current information, radiation pressure is a potential driving mechanism for the outflowing gas in NGC 1377, but the fit is far from perfect and other processes cannot be excluded.

3.3.3. AGN or starburst?

We used the Graham et al. (2011, their Figs. 2–4 and Table 2) calibration of the stellar velocity dispersion and black hole (BH) mass to estimate the mass of a supermassive black hole (SMBH) in NGC 1377. Wegner et al. (2003) listed a value of the stellar velocity dispersion of $\sigma = 83$ km s^{-1} for NGC 1377 in their online database. This gives an SMBH mass in the range of about 4×10^5–6×10^6 $M_\odot$ with a most likely value of about 1.5×10^6 $M_\odot$. If the FIR emission observed were caused by accretion onto the SMBH, it would then operate at ~10% of its Eddington limit. A small acceleration region is consistent with a compact source of energy and momentum. Radiation pressure acceleration minimizes hard shocks, which results in low radio emission and acts on dense gas, consistent with the IR H_2 emission and the suggested ^{12}CO 2–1 molecular outflow. It is also easier to bury a compact energy source behind the gas and dust, giving rise to the deep silicate absorption. Strong FIR emission lines from ionized gas in an AGN are expected to be highly localized around the SMBH, and thus are easier to hide.

In contrast, a dust-enshrouded nuclear starburst needs to be located well inside a radius of 29 pc (to launch the outflow). The current molecular mass here is estimated to be 1.7×10^7 $M_\odot$, 40% of the dynamical mass. Roussel et al. (2006) suggested a starburst with a mass 1.6×10^7 $M_\odot$ assuming an age of 1 Myr, a Salpeter initial mass function (IMF) between 0.1 and 120 $M_\odot$ and 3×10^4 O-stars to produce the bolometric luminosity of NGC 1377. The star formation efficiency (SFE) of the starburst then had to be at least 50% and all of its Paα, and Brγ emission has to be absorbed. This implies that the stars must be deeply buried inside the nuclear dust cloud, putting even stricter limits on their radial distribution. In addition, the starburst scenario requires that almost the entire stellar mass in the center of NGC 1377 has to be very young.

3.4. Comparison with other molecular outflows

Outflowing molecular gas has been detected toward several galaxies of various luminosities. In some cases the existence of an outflow has been inferred from ^{12}CO line wings – such as for the luminous infrared galaxy (LIRG) NGC 3256 (Sakamoto et al. 2006). In some cases, the molecular outflow was discovered in already iconic optical outflows, such as M 82 (Nakai et al. 1987; Walter et al. 2002). There is also mounting evidence of massive, $V \gtrsim 1000$ km s^{-1} outflows in AGN/starburst driven ultra luminous infrared galaxies (ULIRGs) (e.g. Sakamoto et al. 2009; Feruglio et al. 2010; Chung et al. 2011; Sturm et al. 2011; Aalto et al. 2012).

NGC 1377 can also be compared to the AGN-driven molecular outflow of the S0 galaxy NGC 1266 (Alatalo et al. 2011). Nuclear gas depletion time scales are similar to those estimated for NGC 1377, and both galaxies have compact, $r < 100$ pc nuclear disks confining the outflowing wind. NGC 1266 is more FIR luminous than NGC 1377 with an order of magnitude more molecular gas and a factor of five greater gas surface density in its molecular disk. Also, NGC 1266 is not radio deficient ($q = 2.3$), unlike NGC 1377. Estimating the power of a radio jet from the total radio flux, Alatalo et al. (2011) attributed the molecular outflow to the mechanical work of the radio jet of the AGN (see also Matsushita et al. 2007, for a similar case).

What sets NGC 1377 apart are its unusual IR and radio properties, suggesting that the nuclear activity is in a transient phase of its evolution or that NGC 1377 is exceptional in some other aspect. This is illustrated by the fact that observationally the q parameter is in a strikingly small range in large statistical samples of galaxies. In particular, the upper-bound of q is very clear and $q > 3$ is indeed exceptional (see for example Fig. 6 of Yun et al. 2001).

Comparing the energy and mechanical luminosity of the NGC 1377 outflow to one AGN-driven (NGC 1266) and one starburst-driven (NGC 3256) outflow we find them to be similar (within factor of a few). The ratio between the wind luminosity and the FIR luminosity $L_{\rm mech}/L_{\rm FIR}$, however, for NGC 1377 is similar to, or higher than, that of NGC 1266, and at least one order of magnitude higher than that of the starburst driven outflow of NGC 3256. More studies will show if this difference is related to the underlying driving mechanism. The $L_{\rm mech}$ is calculated only on the molecular flows in all three galaxies.

3.5. Nuclear gas properties

3.5.1. Is there a Compton-thick nuclear dust and gas cloud?

For NGC 1377 to hide its power source also at X-ray wavelengths large columns of absorbing material have to reside in front of the nucleus. We estimate the average $N(H_2)$ in the inner $r = 29$ pc of NGC 1377 to be 3.2×10^{23} cm^{-2}. (This corresponds to an A_V of 290 (for N_H(cm^{-2}) = $(2.21 \pm 0.09) \times 10^{21} A_V$, Güver & Özel 2009.) For an absorber to be Compton-thick, an $N_H > 10^{24}$ cm^{-2} ($A_V > 450$) is required. Thus, a Compton-thick absorber, if any, should be smaller than our beam. If the ^{12}CO luminosity of our ^{12}CO 2−1 beam is located in a region with a radius $\lesssim$17 pc, the resulting N_H would be $\gtrsim 10^{24}$ cm^{-2}.

3.5.2. Gas physical conditions

We find a peak ^{12}CO 2−1 temperature of 19 K in a 58 pc beam, which serves as a strict lower limit to the gas kinetic temperature in this region. The dust temperature is difficult to determine but a fit to the 25−100 μm data results in a black body temperature of 80 K with a diameter of 37 pc (Roussel et al. 2003). Comparing our 1 mm continuum flux to the FIR SED suggests it is consistent with a ν^3 slope – either implying $\beta = 1$ – or that the dust is already opaque at $\lambda = 100$ μm. This possibility, if confirmed, would be consistent with the dusty opaque core suggested from the deep silicate absorption. There is no evidence of an excess of 1 mm flux emerging from cold (10−20 K) dust.

We can consider three simple scenarios for the physical conditions of the nuclear molecular gas:

1. *The molecular gas is cold and optically thick.* The ^{12}CO 2−1 emission is optically thick, fills the central beam and its brightness temperature traces the kinetic temperature of the gas at 29 pc radius from the nucleus. This requires a very steep, radial temperature gradient to allow for the buried warm dust.
2. *The molecular gas is optically thin.* In this scenario, the ^{12}CO 2−1 brightness temperature does not reflect the kinetic temperature of the gas even if it fills the central beam and will instead be $\propto T_{\rm ex}\tau$. Given the large columns of absorbing gas and dust, this scenario seems unlikely.
3. *The molecular gas is warm and optically thick* A molecular medium of warm gas clumps that only fills a fraction of the beam. Alternatively, the ^{12}CO peak is unresolved in the beam. If we assume that the emission is emerging from the same region as the inferred dust diameter (of 37 pc), the peak ^{12}CO surface brightness temperature would be 50 K.

The above scenarios assume a single-component ensemble of clouds. A more realistic view of the nuclear molecular ISM is that it likely consists of both dense ($n > 10^4$ cm^{-3}) gas clumps embedded in a lower density ($n = 10^2$−10^3 cm^{-3}) molecular medium (see discussion in e.g. Aalto et al. 1994). The ^{12}CO 2−1 brightness will then reflect the relative filling factor of the low- and high density gas. The detection of bright HCN 1−0 emission (Imanishi et al. 2009) towards the inner 2″ of NGC 1377 suggests gas densities $>10^4$ cm^{-3} (unless the HCN is IR-pumped).

Is the molecular gas concentration forming stars? From the Kennicutt-Schmidt (KS) relation (Kennicutt 1998) the expected SFR from the nuclear gas concentration is 0.1 $M_\odot$ yr^{-1}. This falls short by factors of 4−18 to explain the inferred SFR if all FIR emission is emerging from star formation. However, the KS relation at $r < 100$ pc may have a large scatter because star formation is unlikely to be a steady-state process on such small scales (e.g. Onodera et al. 2010). There should be some star formation going on even if it is difficult to infer the actual SFR.

3.6. The evolutionary implications for NGC 1377

3.6.1. Origin of the molecular gas

Just as for NGC 1266 (Alatalo et al. 2011), one question for NGC 1377 is how the gas reached the very center of the galaxy so efficiently. So far, no clear evidence of an interaction has been presented. The range of possible PAs of the nuclear disk includes a difference by about 40° compared to the stellar disk of NGC 1377. An inclination difference between the gas and stellar disks would indeed suggest an external source for the gas (Davis et al. 2011). It is interesting that the evidence so far suggests that most of the gas has ended up in molecular form. If NGC 1377 accreted a late-type dwarf galaxy or gas from the outer regions of a large disk galaxy, the gas is more likely to be atomic. Somehow the gas must have become shocked and compressed along the way. However, the lack of 1.4 GHz radio continuum emission makes it difficult to assess the amount of cold atomic hydrogen in the center of NGC 1377 – which normally could be tested by searching for absorption in the 21 cm HI line.

The gas concentration may instead be the result of slow, secular evolution such as accretion along a bar (e.g. Jogee et al. 2005), very slow external accretion (galaxy harassment), or stellar return (e.g. Welch & Sage 2003). All of these – or combinations of them – are possible scenarios, but the problem remains of transporting such a concentration of molecular gas to the core of NGC 1377.

3.6.2. The nuclear activity

Observing the molecular properties of NGC 1377 allow us to probe the early stages of nuclear activity and feedback mechanisms in active galaxies. Depending on what is driving the FIR emission and outflow of NGC 1377, we are either witnessing the growth and feeding of a black hole in an early-type galaxy – a process fueled by the late influx of molecular gas. Alternatively, the gas fuels the early triggering phase of a nuclear starburst, increasing the stellar mass instead of the central black hole.

Another important key to the evolutionary stage and nature of the activity is the age of the outflow. If the SMA data recover the full extent of the outflow, this sets an upper limit to its age of 1.4 Myr. High sensitivity observations of ^{12}CO 1−0 as well as deep imaging of dust absorption features, Hα and a search for HI will help determine if the outflow extends beyond the ^{12}CO 2−1 emission. This evidence would additionally constrain the age of a buried power source. An implicit assumption here is that this activity is a one-time event (i.e., not recurrent in a short time scale). The ongoing, mass outflow rate would clear the central region of gas within the short time period of 5−25 Myr. The growth of the SMBH and/or nuclear star formation will cease within this time period. However, if the gas is unable to escape the galaxy, we might be observing a fountain or a failed wind (e.g. Dorodnitsyn et al. 2011). The gas may then fall back onto the galaxy again where the returned gas serves as a reservoir for future activity. Future studies will address this possible evolutionary scenario.

4. Conclusions

We have imaged ^{12}CO and ^{13}CO 2–1 in the FIR-excess galaxy NGC 1377 with the SMA and summarize our results:

1. We found bright, complex ^{12}CO 2−1 line emission from the nuclear region of the FIR-excess S0 galaxy NGC 1377, the structure of which is reminiscent of a disk-outflow system. The ^{12}CO 2−1 line wings, the spatial orientation of the wing-emission with respect to the line-center emission, its correspondence with the optical dust features and the X-shape of the integrated intensity and dispersion maps support this interpretation. Estimated outflow parameters are $M_{\rm out}({\rm H_2}) > 1 \times 10^7\ M_\odot$; $\dot{M} > 8\ M_\odot\,{\rm yr}^{-1}$; $V_{\rm out} > 140\ {\rm km\,s^{-1}}$; extent ≈ 200 pc; opening angle = 60°−70°; PA ≈ 40° and an age of $\sim 1.4 \times 10^6$ yr.
2. We suggest that the age of the outflow supports the notion that the nuclear activity is young – a few Myr. The dusty center of NGC 1377, the lack of significant numbers of recent supernovae, or of a dominant hot wind, may imply that the outflow is driven by radiation pressure from a compact, dust enshrouded nuclear source. However, other driving mechanisms are possible. Accretion onto a $10^6\ M_\odot$ SMBH – i.e. a buried AGN – is a possible power source. Alternatively, the photons may emerge from a very young (1 Myr), pre-supernova starburst, but we find this explanation less likely because of the extreme requirements of compactness and youth of the source. The implied mass outflow rate is sufficiently high to clear the nuclear region of gas within 5−25 Myr and will, at least temporarily, shut off the nuclear activity and growth. If the outflowing gas rains back onto the galaxy it may serve as fuel for a future period of nuclear activity and/or star formation.
3. Molecular masses were estimated through the adoption of a standard ^{12}CO to H_2 conversion factor – with all implied uncertainties. In the whole ^{12}CO 2−1 map we detect $M({\rm H_2}) = 1.5 \times 10^8\ M_\odot$ and in the inner $r = 29$ pc $M({\rm H_2})$ is estimated to $1.7 \times 10^7\ M_\odot$ with an H_2 column density of $N({\rm H_2}) = 3.4 \times 10^{23}\ {\rm cm^{-2}}$. This is not sufficient for the core to be Compton thick and a Compton-thick absorber, if any, is therefore probably smaller than our beam. The average molecular gas surface density within $r = 29$ pc is $\Sigma = 5 \times 10^3\ M_\odot\,{\rm pc^{-2}}$.
4. The ^{12}CO 2–1 brightness temperature sets a lower limit to the nuclear gas kinetic temperature of 19 K, but if cloud filling factors are less then unity, gas temperatures will be significantly higher.

Acknowledgements. The Submillimeter Array is a joint project between the Smithsonian Astrophysical Observatory and the Academia Sinica Institute of Astronomy and Astrophysics and is funded by the Smithsonian Institution and the Academia Sinica. J.S.G. thanks the US National Science Foundation for partial support of this work through NSF grant AST-0708967 to the University of Wisconsin-Madison. S.A. thanks the Swedish Research Council for support (grant 621-2011-4143). K.S. is supported by the Taiwan NSC grant 99-2112-M-001-011-MY3. S.M. acknowledges the co-funding of this work under the Marie Curie Actions of the European Commission (FP7-COFUND).

References

Aalto, S., Booth, R. S., Black, J. H., Koribalski, B., & Wielebinski, R. 1994, A&A, 286, 365
Aalto, S., Garcia-Burillo, S., Muller, S., et al. 2012, A&A, 537, A44
Alatalo, K., Blitz, L., Young, L. M., et al. 2011, ApJ, 735, 88
Chung, A., Yun, M. S., Naraynan, G., Heyer, M., & Erickson, N. R. 2011, ApJ, 732, L15
Condon, J. J. 1992, ARA&A, 30, 575
Davis, T. A., Alatalo, K., Sarzi, M., et al. 2011, MNRAS, 417, 882
de Vaucouleurs, G., de Vaucouleurs, A., Corwin, Jr., H. G., et al. 1991, Third Reference Catalogue of Bright Galaxies (New York, NY, USA: Springer)
Dorodnitsyn, A., Bisnovatyi-Kogan, G. S., & Kallman, T. 2011, ApJ, 741, 29
Feruglio, C., Maiolino, R., Piconcelli, E., et al. 2010, A&A, 518, L155
Graham, A. W., Onken, C. A., Athanassoula, E., & Combes, F. 2011, MNRAS, 412, 2211
Güver, T., & Özel, F. 2009, MNRAS, 400, 2050
Heisler, C. A., & Vader, J. P. 1994, AJ, 107, 35
Helou, G., Soifer, B. T., & Rowan-Robinson, M. 1985, ApJ, 298, L7
Imanishi, M. 2006, AJ, 131, 2406
Imanishi, M., Nakanishi, K., Tamura, Y., & Peng, C. 2009, AJ, 137, 3581
Jogee, S., Scoville, N., & Kenney, J. D. P. 2005, ApJ, 630, 837
Kennicutt, Jr., R. C. 1998, ApJ, 498, 541
Krips, M., Neri, R., García-Burillo, S., et al. 2008, ApJ, 677, 262
Laureijs, R. J., Watson, D., Metcalfe, L., et al. 2000, A&A, 359, 900
Leitherer, C., Schaerer, D., Goldader, J. D., et al. 1999, ApJS, 123, 3
Martin, C. L. 2005, ApJ, 621, 227
Matsushita, S., Muller, S., & Lim, J. 2007, A&A, 468, L49
Murray, N., Quataert, E., & Thompson, T. A. 2005, ApJ, 618, 569
Nakai, N., Hayashi, M., Handa, T., et al. 1987, PASJ, 39, 685
Narayanan, D., Krumholz, M. R., Ostriker, E. C., & Hernquist, L. 2012, MNRAS, 2537
Onodera, S., Kuno, N., Tosaki, T., et al. 2010, ApJ, 722, L127
Paglione, T. A. D., Wall, W. F., Young, J. S., et al. 2001, ApJS, 135, 183
Roussel, H., Helou, G., Beck, R., et al. 2003, ApJ, 593, 733
Roussel, H., Helou, G., Smith, J. D., et al. 2006, ApJ, 646, 841
Sakamoto, K., Ho, P. T. P., & Peck, A. B. 2006, ApJ, 644, 862
Sakamoto, K., Aalto, S., Wilner, D. J., et al. 2009, ApJ, 700, L104
Spoon, H. W. W., Marshall, J. A., Houck, J. R., et al. 2007, ApJ, 654, L49
Sturm, E., González-Alfonso, E., Veilleux, S., et al. 2011, ApJ, 733, L16
Tenorio-Tagle, G., & Munoz-Tunon, C. 1998, MNRAS, 293, 299
Veilleux, S., Shopbell, P. L., & Miller, S. T. 2001, AJ, 121, 198
Wada, K., & Tomisaka, K. 2005, ApJ, 619, 93
Walter, F., Weiss, A., & Scoville, N. 2002, ApJ, 580, L21
Wegner, G., Bernardi, M., Willmer, C. N. A., et al. 2003, AJ, 126, 2268
Welch, G. A., & Sage, L. J. 2003, ApJ, 584, 260
Yun, M. S., Reddy, N. A., & Condon, J. J. 2001, ApJ, 554, 803